The GSMaP Precipitation Retrieval Algorithm for Microwave Sounders—Part I: Over-Ocean Algorithm

Shoichi Shige, *Member, IEEE*, Tomoya Yamamoto, Takeaki Tsukiyama, Satoshi Kida, Hiroki Ashiwake, Takuji Kubota, *Member, IEEE*, Shinta Seto, Kazumasa Aonashi, and Ken'ichi Okamoto, *Member, IEEE*

***Abstract*—We develop an over-ocean rainfall retrieval algorithm for the Advanced Microwave Sounding Unit (AMSU) based on the Global Satellite Mapping of Precipitation (GSMaP) microwave radiometer algorithm. This algorithm combines an emission-based estimate from brightness temperature (Tb) at 23 GHz and a scattering-based estimate from Tb at 89 GHz, depending on a scattering index (SI) computed from Tb at both 89 and 150 GHz. Precipitation inhomogeneities are also taken into account. The GSMaP-retrieved rainfall from the AMSU (GSMaP_AMSU) is compared with the National Oceanic and Atmospheric Administration (NOAA) standard algorithm (NOAA_AMSU)-retrieved data using Tropical Rainfall Measuring Mission (TRMM) data as a reference. Rain rates retrieved by GSMaP_AMSU have better agreement with TRMM estimates over midlatitudes during winter. Better estimates over multitudes over winter are given by the use of Tb at 23 GHz in the GSMaP_AMSU algorithm. It was also shown that GSMaP_AMSU has higher rain detection than NOAA_AMSU.**

***Index Terms*—Microwave radiometer (MWR), microwave sounder, precipitation, rain-rate retrieval.**

I. Introduction

RAIN maps have been produced using data from passive microwave radiometers (MWRs) currently in orbit such as the Tropical Rainfall Measuring Mission (TRMM) Microwave Imager (TMI) [1], the Advanced Microwave Scanning Radiometer for the Earth Observing System (AMSR-E) aboard the National Aeronautics and Space Administration (NASA) Aqua satellite [2], and the Special Sensor Microwave/Imager (SSM/I) aboard satellites of the Defense Meteorological Satellite Program [3], [4]. Information obtained by the TRMM precipitation radar (PR) [5]–[7] accelerated the development of rainfall retrieval from spaceborne passive MWRs. One algorithm using precipitation-related variable models and retrieval methods based on TRMM observation studies is the Global Satellite Mapping of Precipitation (GSMaP) MWR algorithm (hereinafter referred to as GSMaP_MWR) [8], [9].

Despite the improved rainfall estimates using data from passive MWRs, the challenge remains to further fill information gaps through more frequent satellite observations. One way to fill gaps is to use infrared (IR) data, which is available frequently over most areas of the globe from geostationary and polar-orbiting satellites. High-temporal-resolution interpolation for GSMaP_MWR is obtained by cloud-top motion derived from two successive IR images and Kalman filter (hereinafter referred to as GSMaP_MVK) [10]. However, the relationship between cloud-top motion and precipitation feature motion is complex [11], possibly leading to errors.

Passive MWRs are generally of two types: imagers and sounders. Imagers such as the TMI, AMSR-E, and SSM/I have channels suitable for monitoring precipitation. Sounders such as the Advanced Microwave Sounding Unit (AMSU) [12], [13] aboard the National Oceanic and Atmospheric Administration (NOAA) satellites and the first satellite of the Meteorological Operational satellite program (MetOp-A) are primarily developed for profiling atmospheric temperature and moisture using opaque spectral regions. To optimize the sensor performance, 20 channels are divided among three separate total-power radiometers, namely, AMSU-A1, AMSU-A2, and AMSU-B (NOAA-18 and MetOp-A replaced AMSU-B with the similar Microwave Humidity Sounder). Each radiometer uses a cross-track scanner to view the Earth, where AMSU-A1 and AMSU-A2 (denoted collectively as AMSU-A) have fields of view (FOVs) of 48 km at nadir and 149 km $\times$ 79 km at limb, while AMSU-B has FOVs of 16 km at nadir and 52 km $\times$ 27 km at limb. The window channels at 23.8, 31.4, 50.3, 89, and 150 GHz are used to retrieve several important parameters related to the hydrological cycle and expand the AMSU capability beyond that of temperature and moisture profiling [14].

Two AMSU-based rainfall retrieval algorithms have been developed. One is a neural-network-based algorithm developed at the Massachusetts Institute of Technology, Cambridge [15], [16]. The algorithm is trained using a cloud-resolving model. The other is the Microwave Surface and Precipitation Products System (MSPPS) Day-2 rainfall algorithm for the AMSU and has been developed at NOAA (hereinafter referred to as

Manuscript received October 1, 2008; revised February 19, 2009. First published June 5, 2009; current version published August 28, 2009. This work was supported by the Japan Aerospace Exploration Agency under the 5th TRMM RA.

S. Shige, T. Yamamoto, T. Tsukiyama, S. Kida, and H. Ashiwake are with the Department of Aerospace Engineering, Osaka Prefecture University, Sakai 599-8531, Japan (e-mail: shige@aero.osakafu-u.ac.jp; tomoya@aero.osakafu-u.ac.jp; t-tsukiyama@aero.osakafu-u.ac.jp; kida@aero.osakafu-u.ac.jp; h-ashiwake@aero.osakafu-u.ac.jp).

T. Kubota is with the Earth Observation Research Center, Japan Aerospace Exploration Agency, Tsukuba 305-8505, Japan (e-mail: kubota.takuji@jaxa.jp).

S. Seto is with the Institute of Industrial Science, The University of Tokyo, Tokyo 153-8505, Japan (e-mail: seto@rainbow.iis.u-tokyo.ac.jp).

K. Aonashi is with the Forecast Research Department, Meteorological Research Institute, Japan Meteorological Agency, Tsukuba 305-0052, Japan (e-mail: aonashi@mri-jma.go.jp).

K. Okamoto was with the Department of Aerospace Engineering, Osaka Prefecture University, Sakai 599-8531, Japan. He is now with the Faculty of Environmental and Information Studies, Tottori University of Environmental Studies, Tottori 689-1111, Japan (e-mail: kokamoto@kankyo-u.ac.jp).

Color versions of one or more of the figures in this paper are available online at http://ieeexplore.ieee.org.

Digital Object Identifier 10.1109/TGRS.2009.2019954

NOAA_AMSU) [14]. Because there have been four AMSU instruments in orbit since the launch of NOAA18 in May 2005, together with five microwave imagers (TMI, AMSR-E, and SSM/I), there have been more observations of rainfall in time and space, with swaths being ∼2200 km wide. Another advantage of the four AMSU sensors on the NOAA satellites and MetOp-A is that they are typically spaced about 4 h in time, thus giving a better representation of the diurnal cycle. Three AMSU sensors have been incorporated into high-spatial- and temporal-resolution precipitation products such as the TRMM Multisatellite Precipitation Analysis (TMPA) [17], Climate Precipitation Center Morphing Technique (CMORPH) [18], and Naval Research Laboratory Blended Satellite Technique (NRL-Blended) [19], [20]. Different precipitation retrieval algorithms are applied to different passive microwave radiometric sensors for subsequent use in these high-resolution precipitation products. For example, in the current TMPA, passive microwave FOVs from the TMI, AMSR-E, and SSM/I are converted to precipitation estimates at the TRMM Science Data and Information System (TSDIS) with sensor-specific versions of the Goddard profiling (GPROF) algorithm [21]–[24], while those from AMSU are converted to precipitation estimates at the National Environmental Satellite, Data, and Information Service (NESDIS) with the NOAA_AMSU algorithm [14].

In this paper, we develop a rainfall retrieval algorithm for AMSU (hereinafter referred to as GSMaP_AMSU) that shares at a maximum a common algorithm framework with the GSMaP_MWR algorithm [8], [9]. An hourly global rainfall map in near real time (about 4 h after observation) based on the GSMaP algorithm [8]–[10] has been provided by the Japan Aerospace Exploration Agency (JAXA)/Earth Observation Research Center [25]. In the current system, high-temporal-resolution interpolation of the rainfall estimated using data from microwave imagers (TMI, AMSR-E, and SSM/I) is obtained using the IR information. Offline tests showed that the IR interpolation of GSMaP (GSMaP_MVK) is more efficient using rain estimations derived from microwave sounder data based on the NOAA_AMSU algorithm in addition to those derived from microwave imager data [26]. The NOAA_AMSU algorithm is a scattering algorithm that mainly relies on data from AMSU-B channels, as will be described later (Section II-B). Over land, only the scattering-based algorithm can be used because the contrast between surface and atmosphere becomes less owing to high emissivity over land, making it difficult to apply the emission-based algorithm. On the other hand, over ocean, both the emission- and the scattering-based algorithm can be used because of low emissivity over ocean. Here, we develop rain retrieval over ocean for the GSMaP_AMSU algorithm, which combines an emission-based estimate from brightness temperature (Tb) data at 23 GHz and a scattering-based estimate from Tb data at 89 GHz.

II. Data

A. Space–Time Matchup of AMSU Data Against TRMM Data

In principle, rainfall retrievals using data from the PR and TMI aboard the TRMM satellite are superior to those using data from AMSU instruments, which have coarser FOVs and channels for profiling atmospheric temperature and moisture instead of precipitation. The PR provides height information based upon the time delay of the precipitation-backscattered return power and allows vertical profiles of precipitation to be obtained directly. The TMI is equipped with channels suitable for monitoring precipitation; in particular, a 10-GHz channel has a nearly linear relationship between brightness temperatures and rain rate. Thus, a comparison of AMSU estimates against TRMM estimates is very useful for the development and validation of AMSU rainfall retrievals. In this paper, we matched TRMM rainfall products and NOAA-15, NOAA-16, and NOAA-17 AMSU retrievals over ocean for two months of January and July 2005. A total of 75 significant rain events (44 events for January 2005 and 31 events for July 2005) for matched TRMM-AMSU orbits were found within a 20-min window. When instantaneous imagery was compared, either PR or TMI estimates were averaged for the AMSU-B FOV. The antenna pattern for the AMSU-B was approximated by a Gaussian weighting function with the same 3-dB beam width as for the actual antenna pattern. We applied the rainfall retrieval algorithm (GSMaP_AMSU) to the matched AMSU/TRMM data and validated the estimates using the GSMaP_MWR estimates from the TMI data (hereinafter referred to as GSMaP_TMI) as references. We also used the current (version 6) level-2 standard products of the PR and TMI, which are published by NASA and JAXA. The level-2 standard product 2A12 (GPROF algorithm) was used for the rain estimation from the TMI data [22], [23]. The basis of GPROF is a Bayesian framework, in which retrieved precipitation is constructed from cloud-resolving model-generated profiles that are radiatively consistent with the observation [21]. The level-2 standard product 2A25 was used for the rain estimation from the PR data [27]–[29]. The PR operates at a single frequency of 13.8 GHz so that the PR2A25 algorithm corrects the attenuation in the measured radar reflectivity factor Zm and estimates the attenuation-corrected radar reflectivity factor Ze. The attenuation correction is based on a hybrid method that provides a smooth transition between the Hitschfeld–Bordan [30] method, which performs well at low attenuations, and the surface reference technique [31], for which the relative error decreases with increasing path-integrated attenuation. This method is termed the "a-adjustment" method [32].

B. NOAA_AMSU (MSPPS Day-2) Rainfall Algorithm

The MSPPS Day-2 rainfall algorithm for the AMSU (NOAA_AMSU) was developed at NOAA [14]. The algorithm originates from the works of Weng and Grody [33] and, subsequently, Zhao and Weng [34]. A simultaneous retrieval of the ice water path (IWP) and ice-particle effective diameter (De) from Tb data at 89 and 150 GHz was performed through two processes: simplifying the radiative transfer equation into a two-stream approximation and estimating the cloud-base and cloud-top Tbs through the use of AMSU measurements at 23.8 and 31.4 GHz. The rain rate was computed based on an IWP and rain-rate relation derived from the GPROF algorithm database, which contains the profiles of various hydrometeors generated from the cloud-resolving models.

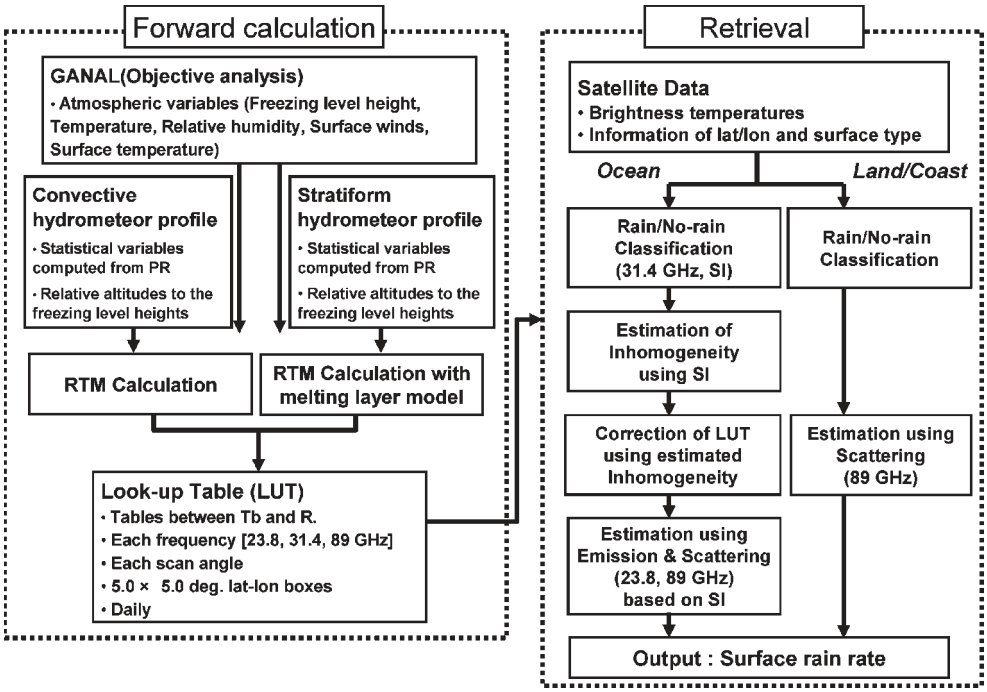

Fig. 1. Flowchart for the GSMaP_AMSU rain retrieval algorithm in this paper.

The weakness of the NOAA_AMSU algorithm is that only precipitation that is detectable from a scattering signature can be estimated [17], [18]. Recently, a new correction has been developed for the AMSU-A cloud liquid water content to fill in the gaps of NOAA_AMSU retrievals over ocean [35]. In this paper, rain estimates derived using the improved NOAA_AMSU algorithm were used.

C. GSMaP_MWR Algorithm

The GSMaP_MWR algorithm is a PR-consistent advanced MWR algorithm [8], [9]. The basic idea of the GSMaP_MWR algorithm is to find the optimal rainfall that gives radiative transfer model (RTM) FOV-averaged Tbs that fit best the observed Tbs [36], [37]. The GSMaP_MWR algorithm consists of the forward calculation part to calculate the lookup tables (LUTs) showing the relationship between rainfall rates and Tbs with an RTM, and the retrieval part to estimate precipitation rates from the observed Tbs using the LUTs. The forward calculation part of the GSMaP_MWR algorithm, which the GSMaP_AMSU algorithm shares with the GSMaP_MWR algorithm (Fig. 1), is described in detail.

The RTM calculation requires information on atmospheric variables, as well as precipitation-related variables. Atmospheric temperature, freezing-level height (FLH), surface winds, and surface temperature are adapted from the Japan Meteorological Agency (JMA) global analysis (GANAL). Similarly, sea surface temperature is adapted from JMA merged satellite and *in situ* data global daily sea surface temperatures in the global ocean. As for relative humidity, the constant value of 100% is assumed.

The convective and stratiform precipitation models for precipitation-related variables (hydrometer profiles, drop-size distribution (DSD), etc.) are constructed for ten precipitation types. Precipitation types are determined in terms of stratiform pixel ratio, stratiform rain ratio, precipitation area, precipitation top height, rain intensity, and diurnal cycle from the PR2A25 data, together with the ratio between PR precipitation rates and TRMM lightning imaging sensor flash rates [38]–[40]. Precipitation types consist of six land types (severe thunderstorm, afternoon shower, shallow convection, extratropical cyclone, organized convection, and highland rain) and four ocean types (shallow convection, extratropical cyclone, transition zone, and organized convection). Global distributions of the precipitation types in $2.5^\circ \times 2.5^\circ$ latitude–longitude boxes are statistically classified trimonthly.

The convective and stratiform precipitation profiles of PR2A25 data are averaged over prescribed precipitation ranges for each precipitation type. In this averaging, profiles relative to FLH are used to exclude the influence of atmospheric temperature variations [9]. The database of precipitation types and profiles makes it possible for the algorithm to deal with trimonthly variation of typical hydrometeor profiles.

For rain DSD, a gamma distribution of raindrop size is assumed

$$N(D) = N_0 D^{\mu} \exp(-\Lambda D)$$

where $N(D)$ is the number concentration for particles with diameter D, $\mu = 3$, and N_0 and Λ are the parameters to be determined. For convective precipitation, N_0 and Λ are determined using the DSD parameter estimated from the "a-adjustment" method of the PR2A25 algorithm [41]. For stratiform precipitation, the standard values of N_0 and Λ assumed in the PR2A25 algorithm are used.

On the other hand, conventional models were used for frozen and mixed-phase particle-size distribution that could not be estimated from the TRMM PR observation. The exponential distribution is used for the drop-size distribution model of

snow and graupel. The refractivity of convective and stratiform frozen particles is calculated, assuming them as the mixture of ice and air with an empirically prescribed constant density (200 $\mathrm{kg \cdot m^{-3}}$). Particle-size distribution and refractivity for mixed-phase stratiform precipitation (between FLH minus 1 km and FLH) were parameterized in terms of atmospheric temperature [42], [43], while mixed-phase convective precipitation was neglected.

From forward calculations with a four-stream RTM [44], LUTs showing the relationship between rainfall rates and Tbs were computed daily in $5.0^\circ \times 5.0^\circ$ latitude–longitude boxes. Surface rainfalls have been retrieved from the TMI, SSM/I, AMSR, and AMSR-E using the GSMaP algorithm [45].

III. Algorithm Development

A flowchart of the GSMaP_AMSU algorithm is shown in Fig. 1. Similar to the GSMaP_MWR algorithm and other MWR rain retrievals, the GSMaP_AMSU algorithm consists of two parts: the forward calculations for making the LUTs and the retrievals from the Tb data of satellite-borne MWRs (i.e., AMSU).

A. Forward Calculation

The left panel of Fig. 1 describes the process of making the LUTs. Some modifications have been made to the process of making the LUTs in the GSMaP_MWR algorithm for its application to the AMSU data, taking the differences between imagers and sounders into account. While conical scanning radiometers such as the TMI preferentially scan at a constant slant path angle, the AMSU radiometer uses cross-track scanning to view the Earth. The variations in path lengths through which the atmosphere is viewed by cross-track scanning should be taken into account. For the AMSU, the received polarization also varies with scan angle because of the rotating-reflector/fixed-feed horn antenna design. This is different from that of imagers using a conical scanning mechanism, which receive a fixed polarization independent of the scan. At a given scan angle θ_s, the normalized surface emitted radiation (i.e., emissivity) ε_s seen by the AMSU contains mixed vertical ε_V and horizontal ε_H polarizations (the very small cross-polarized contribution due to imperfect cross-polarization isolation in the antenna is neglected), i.e.,

$$\varepsilon_s = \varepsilon_V(\theta)\cos^2\theta_s + \varepsilon_H(\theta)\sin^2\theta_s \tag{1}$$

where the local zenith angle θ (LZA) varies as a function of scan angle θ_s [46]. The LUTs are produced for each scan angle from RTM calculations using (1). For a sea surface, the emissivity components ε_V and ε_H are calculated using the Fresnel formula for calm seas [47], together with an empirical model that includes the effects of wind-driven foam and surface roughness on emissivity [48], while for a land surface, they are set at 0.9.

Fig. 2 shows an example, used in the GSMaP_AMSU algorithm, of the LUT for Tbs at 23.8 GHz (Tb23), 31.4 GHz (Tb31), 89 GHz (Tb89), and 150 GHz (Tb150) for midlatitudes during winter ("extratropical cyclone over ocean" at the grid point (162.5° E, 32.5° N) on January 1, 2005). The LUT has 60 lines for LZAs between the nadir and limb in intervals of 2°. In the retrieval process, we used values of the LUTs interpolated linearly using the four neighboring boxes.

It is seen from Fig. 2(a) that Tb23 increases with rainfall rate and becomes saturated at a certain rain rate, which decreases with increasing LZA. In this example, the rain rate for saturation is about 12.0 $\mathrm{mm \cdot h^{-1}}$ for LZA $= 0$ (near the nadir), while it is about 10.0 $\mathrm{mm \cdot h^{-1}}$ for LZA $= 60$ (near the limb). Tb31 also increases with rainfall rate but becomes saturated at a smaller rain rate than Tb23 does [Fig. 2(b)]. On the other hand, Tb89 either does not change greatly or decreases with increasing rain rate for this low-rainfall-rate range, as well as Tb150. The main feature of the low-rainfall-rate range is that the increase in rainfall rate increases values of Tb23. The rainfall rate range that is lower than 12.0 $\mathrm{mm \cdot h^{-1}}$ for LZA $= 0$ (10.0 $\mathrm{mm \cdot h^{-1}}$ for LZA $= 60$) is therefore referred to as the "emission regime."

It is also noted that Tb23 at 0 $\mathrm{mm \cdot h^{-1}}$ in the LUTs ($\mathrm{Tb23_{LUT0}}$) for LZA $= 60$ is larger than that for LZA $= 0$ because the path length through which the atmosphere is viewed by cross-track scanners increases with LZA. Here, "diff_$\mathrm{Tb23_{LUT}}$" is defined as follows:

$$\mathrm{diff\_Tb23_{LUT}} = \mathrm{Tb23_{LUTsat}} - \mathrm{Tb23_{LUT0}} \tag{2}$$

where $\mathrm{Tb23_{LUTsat}}$ is Tb23 for saturation in the LUTs. A larger diff_$\mathrm{Tb23_{LUT}}$ for LZA $= 0$ than that for LZA $= 60$ indicates that Tb23 represents rainfall rate more unambiguously, because Tb23 in the LUT increases more rapidly with rainfall. Therefore, diff_$\mathrm{Tb23_{LUT}}$ indicates certainty of the emission-based rainfall retrieval using Tb23, and the variations in diff_$\mathrm{Tb23_{LUT}}$ should be taken into account by the algorithm.

For rainfall rates that are greater than the rain rates for Tb23 saturation, Tb89 decrease rapidly [Fig. 2(c)], while Tb23 slightly decreases with an increase in rainfall rate. Clearly, in this rainfall rate range, the emission for raindrops is no longer a useful indicator of rainfall rate. Only the signal of scattering by ice particles at 89 GHz can provide information on precipitation. Tb150 also decreases with rainfall [Fig. 2(d)]. However, Tb89 is more suited for directly sensing precipitation intensity information within the main rain layers than Tb150, because the response to snow and graupel lowers the Tb and increases strongly with frequency. We refer to the rainfall rate range that is higher than 12.0 $\mathrm{mm \cdot h^{-1}}$ for LZA $= 0$ (10.0 $\mathrm{mm \cdot h^{-1}}$ for LZA $= 60$) as the "scattering regime."

It should be noted that the rainfall rate range of the emission and scattering regimes are not constant and vary for the LUTs, which are computed daily in $5.0^\circ \times 5.0^\circ$ latitude–longitude boxes. Fig. 3 shows the LUTs for low latitudes ("organized convection over ocean" at the grid point (157.5° E, 2.5° N) on January 1, 2005). In this case, the rainfall rate range that is lower than 10.0 $\mathrm{mm \cdot h^{-1}}$ for LZA $= 0$ (3.0 $\mathrm{mm \cdot h^{-1}}$ for LZA $= 60$) is referred to as the "emission regime." It is also noted that $\mathrm{Tb23_{LUT0}}$ for low latitudes [Fig. 3(a)] is higher than $\mathrm{Tb23_{LUT0}}$ for midlatitudes during winter [Fig. 2(a)]. This is because there is a larger amount of water vapor at low latitudes than at midlatitudes during winter. Therefore, diff_$\mathrm{Tb23_{LUT}}$

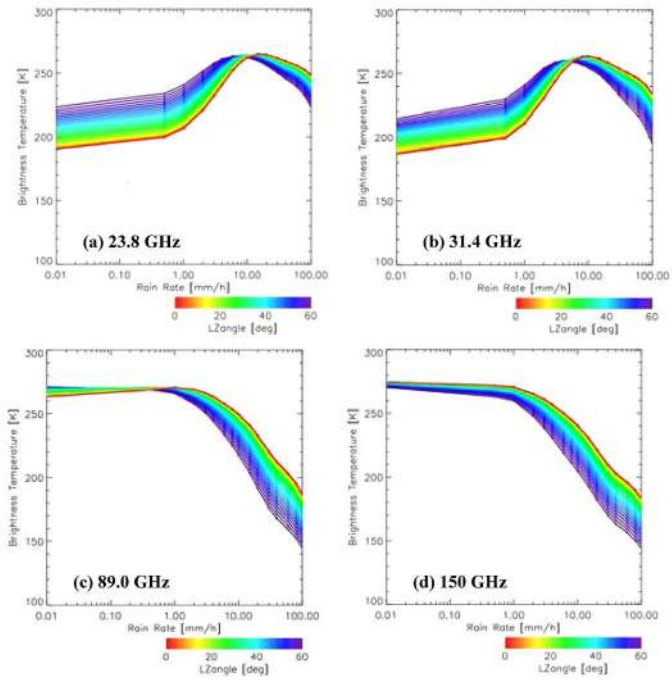

Fig. 2. Examples of Tb LUTs for "extratropical cyclone over ocean" at the grid point (162.5° E, 32.5° N) on January 1, 2005, at (a) 23.8 GHz, (b) 31.4 GHz, (c) 89.0 GHz, and (d) 150 GHz used in the GSMaP_AMSU algorithm. The horizontal and vertical axes denote the rain rates and calculated Tbs, respectively. Color denotes the LZA between the nadir and limb in intervals of 2°, as indicated by the value bar at the bottom of the figures.

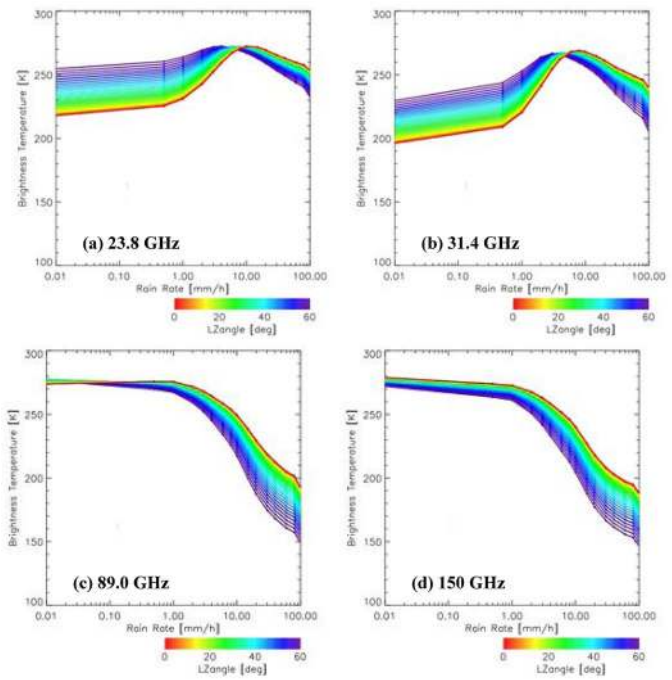

Fig. 3. Same as Fig. 2 except for "organized convection over ocean" at the grid point (157.5° E, 2.5° N) on January 1, 2005.

for low latitudes is smaller than that for midlatitudes during winter, indicating that Tb23 represents rainfall rate more ambiguously.

Radiative transfer calculations that assume homogeneous rainfall distributions fail to properly reproduce the observed

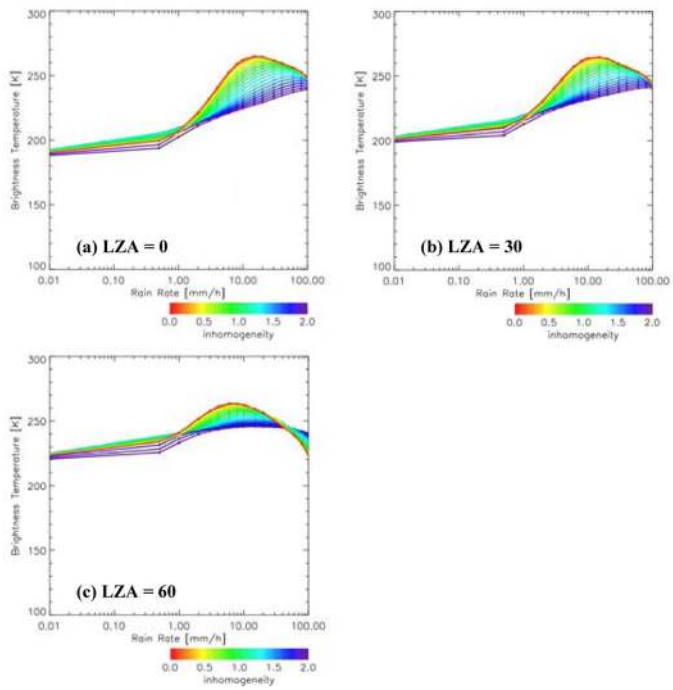

Fig. 4. LUTs for Tbs at 23.8 GHz for LZAs of (a) 0°, (b) 30°, and (c) 60°, corrected using the inhomogeneities for "extratropical cyclone over ocean" at the grid point (162.5° E, 32.5° N) on January 1, 2005, as shown in Fig. 2(a). The horizontal and vertical axes denote the rain rates and calculated Tbs, respectively. Color denotes the precipitation inhomogeneity between zero and two (with steps of 0.1), as indicated by the value bar at the bottom of the figures.

relations between rainfall and brightness temperatures. Precipitation in the real atmosphere is assumed to be lognormally distributed in the horizontal, as observed in [49] and [50]. It is then possible that the RTM-derived Tb–rain relations are modified as a function of the variability ζ using a method similar to the one used in the study of [51] and the GSMaP_MWR algorithm [8], [9]

$$\mathrm{Tb}_{\mathrm{correct}}\left(\langle R\rangle,\zeta\right)=\int_0^\infty \mathrm{Tb}(R)\frac{1}{(2\pi)^{1/2}\zeta R}\times\exp\left\{\frac{-1}{2\zeta^2}\left[\ln(R)-\mu\right]^2\right\}dR \quad (3)$$

where R is the rain rate, $\langle R\rangle$ is the mean rain rate of the lognormal distribution $\zeta^2=\ln(\sigma^2+1)^2$, with σ being the variability of the rainfall; $\mu=\ln(\langle R\rangle)-0.5\zeta^2$; $\mathrm{Tb}(R)$ is the RTM-derived Tb–rain relation; and $\mathrm{Tb}_{\mathrm{correct}}$ is the Tb–rain relation corrected by the lognormal distribution. Figs. 4 and 5 show the LUTs for Tb23 and Tb89 corrected using ζ from that shown in Fig. 2(a) and (c). It is seen from Fig. 4 that the rain rates for Tb23 saturation increase with the value of ζ, which means that the rainfall rate range of the emission regime is extended.

B. Retrieval

The right panel of Fig. 1 shows the process of retrieving from the AMSU Tbs. Here, we used an Advanced TIROS Operational Vertical Sounder and Advanced Very High Resolution

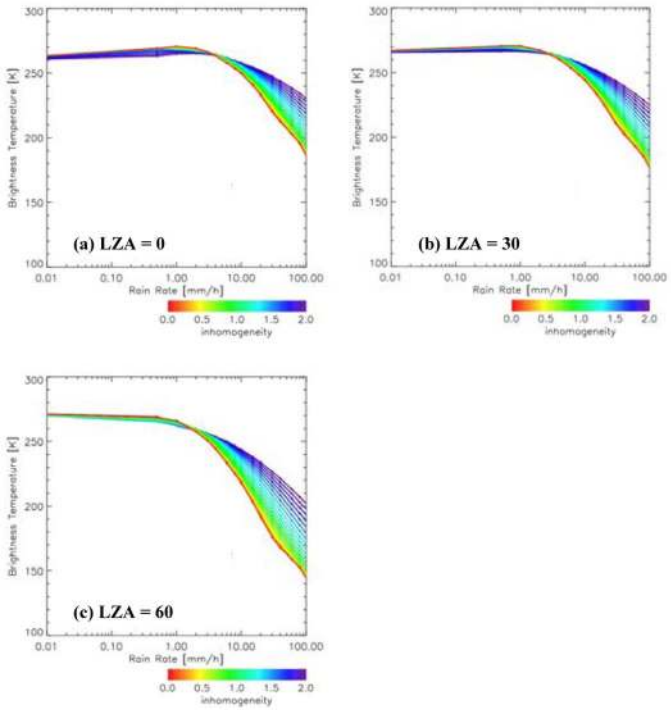

Fig. 5. Same as Fig. 4 except for 89.0 GHz.

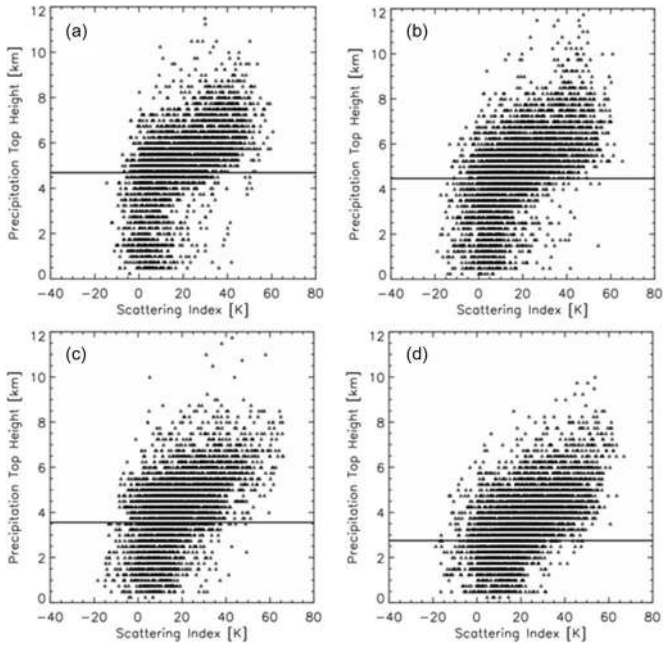

Fig. 6. Precipitation top height observed by the PR plotted versus SI (K) for (a) diff_LUT23 <50 K, (b) 50 K $<$ diff_LUT23 <60 K, (c) 60 K $<$ diff_LUT23 <70 K, and (d) diff_LUT23 >70 K from the 75 AMSU/TRMM matched-up cases. The horizontal lines indicate the FLHs.

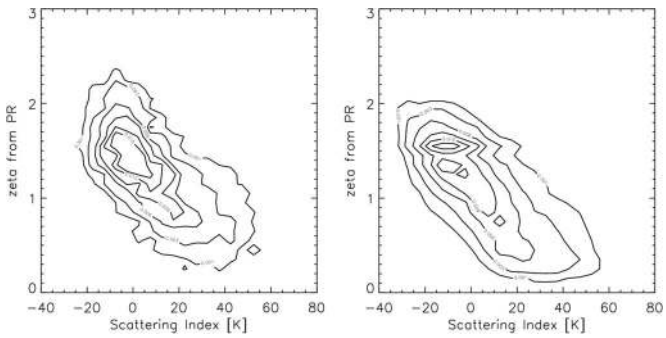

Fig. 7. Two-dimensional probability density functions in terms of (horizontal axis) SI and (vertical axis) ζ for (left) AMSU-A FOV and (right) AMSU-B FOV.

Radiometer Preprocessing Package (AAPP) [52] to obtain the AMSU Tb data. We developed the retrieval process, retaining the basic structure of the GSMaP_MWR algorithm. Emission signatures are mainly used to determine rainfall, while scattering signatures are used to help define the nature of precipitation, similar to the SSM/I algorithm in the study of [53].

Taking advantage of 150 GHz of the AMSU, an SI is defined as follows:

$$\mathrm{SI} = (\mathrm{Tb89} - \mathrm{Tb89}_{\mathrm{LUT0}}) - (\mathrm{Tb150} - \mathrm{Tb150}_{\mathrm{LUT0}}) \quad (4)$$

where $\mathrm{Tb89}_{\mathrm{LUT0}}$ and $\mathrm{Tb150}_{\mathrm{LUT0}}$ are Tb89 and Tb150 at 0 mm $\cdot$ h^{-1} in the LUTs, respectively. Because the response to snow and graupel lowers the Tb and increases strongly with frequency, the Tb reduction is higher at 150 GHz than at 89 GHz [Fig. 2(c) and (d)]. Fig. 6 shows relationships between the SI calculated from AMSU-B data and the PR-observed precipitation top height for each $\mathrm{diff\_Tb23}_{\mathrm{LUT}}$ range. Freezing heights increase with $\mathrm{diff\_Tb23}_{\mathrm{LUT}}$, which is consistent with the comparison of the LUT for midlatitudes during winter [Fig. 2(a)] and that for low latitudes [Fig. 3(a)] in Section III-A. It is seen that thickness between PR precipitation top height and FLH increases with AMSU-B SI. This result is consistent with that from the previous study (see [54, Fig. 3]). In the retrieval process, SI is used to help define the nature of precipitation.

At the beginning of this process, rain or no-rain flags are identified by deterministic methods. The rain/no-rain classification (RNC) over ocean consists of two processes. In the first process, emission signature from Tb31 is utilized, because tests show that utilization of Tb23 results in higher false-alarm ratio (FAR) due to its adjacency to the center of the water-vapor line. Here, FAR is the fraction of positive forecasts that turn out to be wrong. Further definition of FAR is described in the study of [55]. Therefore, over ocean, rain flags are identified as

$$\mathrm{Tb31} \geq \mathrm{Tb31}_{\mathrm{LUT0}} \quad (5)$$

where $\mathrm{Tb31}_{\mathrm{LUT0}}$ is Tb31 at 0 mm $\cdot$ h^{-1} in the LUTs. It should be noted that $\mathrm{Tb31}_{\mathrm{LUT0}}$ is not constant and varies for the LUTs [see Figs. 2(b) and 3(b)]. Using Tb31 allows us to detect warm rain from clouds that lack the ice phase, which account for 31% of the total rain amount and 72% of the total rain area in the tropics [56].

It is shown from Fig. 2(b) that, for large LZA, Tb31 for strong rain rate is smaller than $\mathrm{Tb31}_{\mathrm{LUT0}}$, leading to misclassification of such strong rain pixels as no-rain pixels. Therefore, in the second check, using SI, rain flags are identified as follows:

$$\mathrm{SI} > 0. \quad (6)$$

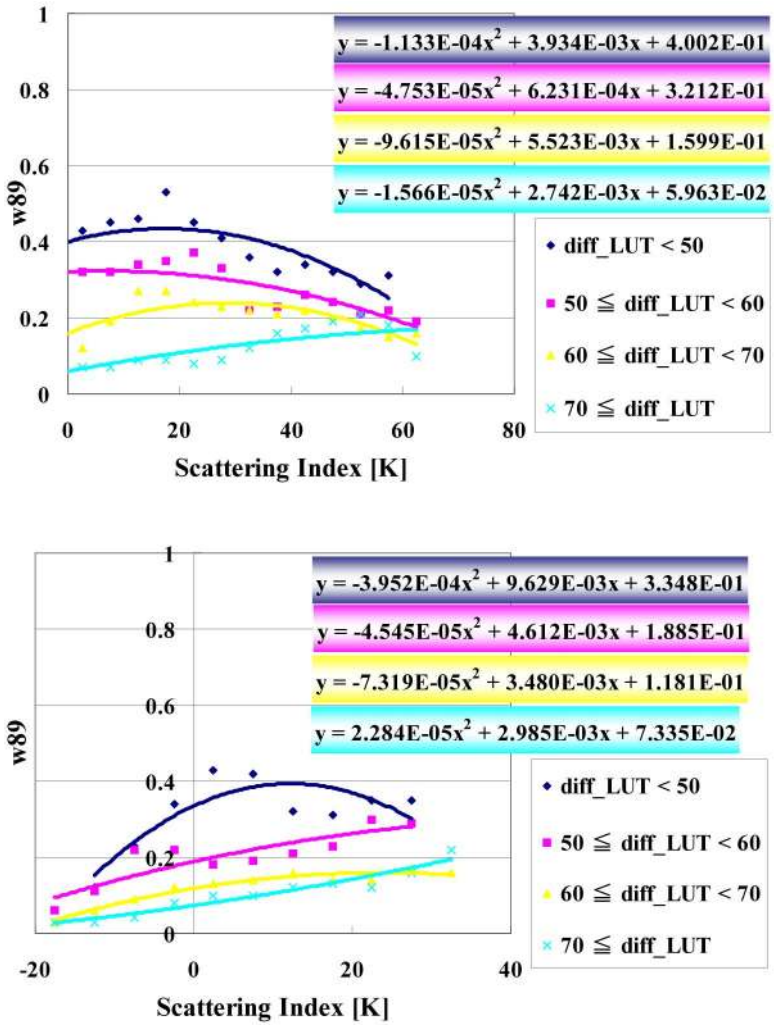

Fig. 8. Weighting function $w89$ giving the smallest rmse between Rain2389 and PR estimate for (top) RN3 and (bottom) the remaining two raining groups (RN1 and RN2) and for each range of diff_Tb23LUT. The weighting function $w89$ is determined based on the AMSU/TRMM matched-up cases and interpolated by quadratic equations.

Therefore, each FOV is separated into the following four groups:

RN0 classified as no-rain pixel by (5) and (6);
RN1 classified as rain pixel only by (5);
RN2 classified as rain pixel only by (6);
RN3 classified as rain pixel by (5) and (6).

As already noted, the horizontal inhomogeneity of rainfall within rather large AMSU FOVs must be taken into account by the algorithm in order to properly compensate for nonlinearities in the Tbs versus water content relationships. Here, the variability of the rainfall σ is defined using rain rates estimated from the PR as

$$\sigma = \frac{\left[\frac{1}{N}\sum_{i=1}^{N}(R_i - R_{\mathrm{avg}})^2\right]^{1/2}}{R_{\mathrm{avg}}} \tag{7}$$

where i represents each pixel of the PR data within the FOV area and N is the total number of pixels in the area. Fig. 7 shows relationships between the SI calculated from AMSU-B data and ζ for the AMSU-A and AMSU-B FOVs computed from PR data. For both AMSU-A and AMSU-B FOVs, ζ decreases with SI. This is explained by the fact that deep convection having large SI is generally embedded in mesoscale convective systems having horizontal scales larger than AMSU-A and AMSU-B FOV sizes. The values of ζ for the AMSU-A and AMSU-B FOVs are estimated from SI based on statistical relationships from Fig. 7 as

$$\begin{aligned} \zeta &= -0.0165SI + 1.4050, \quad \text{for AMSU-A FOV} \\ \zeta &= -0.177SI + 1.0383, \quad \text{for AMSU-B FOV.} \end{aligned} \tag{8}$$

Since AMSU-A and AMSU-B FOV sizes vary with LZA, the aforementioned relationships should be produced for each LZA range. However, feature did not change greatly with LZA range, possibly due to the small number of the AMSU/TRMM matched-up cases. Therefore, variations in AMSU FOV sizes are not taken into account.

The LUTs at 23 and 89 GHz are corrected using the value of ζ estimated from SI for AMSU-A and AMSU-B FOVs, respectively. Using the corrected LUTs, rain rates are retrieved

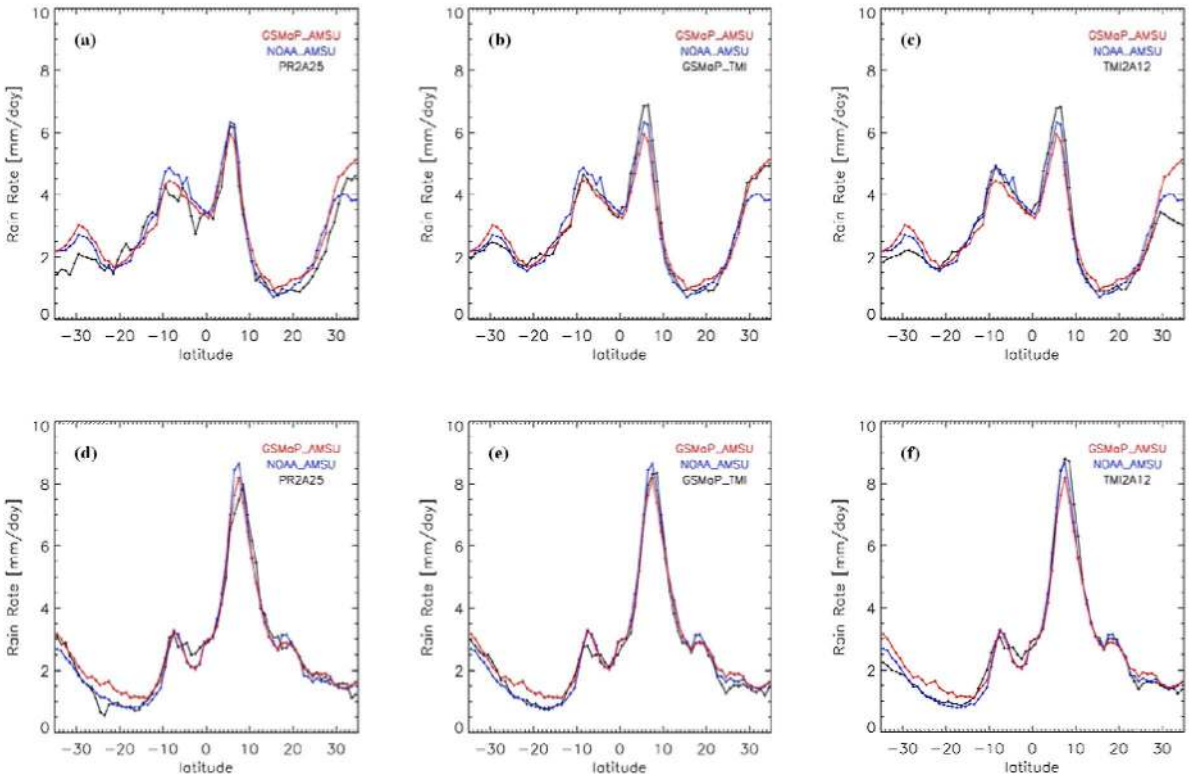

Fig. 9. Zonally averaged rain rates retrieved by GSMaP_AMSU, NOAA_AMSU, and reference algorithm [PR2A25 for (a) and (d), GSMaP_TMI for (b) and (e), and TMI2A12 for (c) and (f)] over ocean only for (a)–(c) January 2005 and (d)–(f) July 2005.

from Tb23 (Rain23) and Tb89 (Rain89). Here, Rain23 and Rain89 are given by the rain rates of Tb23 and Tb89 in the corrected LUT corresponding to the observed Tb23 and Tb89, respectively.

The rainfall estimate at the AMSU-B FOV is given by combining estimates from emission and scattering algorithms as

$$\text{Rain2389} = (1 - w89) \times \text{Rain23} + w89 \times \text{Rain89}. \quad (9)$$

The weighting $w89$ is a function of SI and determined based on the AMSU/TRMM matched-up cases. Fig. 8 shows $w89$ that gives the smallest root-mean-square error (rmse) between Rain2389 and PR estimates for RN3, which is the major raining group, and the remaining two raining groups (RN1 and RN2). The weighting w89 is determined for each range of $\text{diff\_Tb23}_{\text{LUT}}$ and then interpolated by quadratic equations. It should be noted that the nominal and effective resolution that retrievals produced corresponds to the AMSU-B FOV size and varies with LZA.

Only precipitation retrievals over ocean are considered in the current investigation, but those over land and coast are briefly described. Over land, the RNC method, which is based on the probability distribution of Tb under no-rain conditions derived from unclassified AMSU pixels similar to the algorithm of [57], is used. Over coast, the RNC method of [58] is used. The estimate is then given by the rain rate retrieved from Tb89 (i.e., Rain89).

IV. Validation of Rainfall Retrievals

A. Global Scale

Fig. 9 compares zonally averaged rain rates over ocean for GSMaP_AMSU and NOAA_AMSU using PR2A25, GSMaP_TMI, and TMI2A12 as references. Qualitatively, both GSMaP_TMI and NOAA_AMSU have good agreement with the reference algorithms.

Over midlatitudes (30° N–35° N) during winter (January 2005), GSMaP_AMSU has good agreement with GSMaP_TMI [Fig. 9(b)]. On the other hand, NOAA_AMSU gives lower rainfall rates than GSMaP_TMI does but higher rainfall rates than TMI2A12 does. It is noted that GSMaP_AMSU is in very good agreement with PR2A25 for latitudes 30° N–35° N [Fig. 9(a)]. The differences between PR2A25 and TMI2A12 standard rainfall products over midlatitude regions during winter are well known (e.g., [59]). Studies [60]–[62] found biases in the freezing-level estimates [63] used in TMI2A12 retrievals, particularly over midlatitude regions during winter. On the other hand, the freezing heights derived from GANAL are used in GSMaP_TMI. The basis of the TMI 2A12 algorithm is a "Bayesian" framework, in which the retrieved precipitation is constructed from those cloud-resolving model-generated profiles that are radiatively consistent with the observation [21], [22]. Although the cloud-radiative model database supporting the TMI2A12 V6 algorithm has been expanded, the database consists of only six simulations, two of which are extratropical cyclone cases (see [23, Table 2]). On the other hand, in GSMaP_TMI, RTM calculations use a trimonthly database

of precipitation types and profiles in $2.5^\circ \times 2.5^\circ$ latitude–longitude boxes derived from the PR2A25 data. Thus, compared with the supporting databases of the TMI2A12 algorithm, those of the GSMaP_TMI algorithm are more consistent with naturally occurring profiles at the time/location where the algorithm is applied. Furthermore, GSMaP_TMI can detect rainfall events behind cold fronts over midlatitude regions during winter that are consistently missed by TMI2A12 [64]. Thus, it is fair to say that, over midlatitudes during winter, GSMaP_TMI estimates are better than TMI2A12 V6 ones. The upcoming TMI2A12 V7 estimates are larger than TMI2A12 V6 and even larger than PR2A25 V6 over midlatitudes during winter [65]. Therefore, over midlatitudes during winter, GSMaP_AMSU, which has better agreement with GSMaP_TMI, is better than NOAA_AMSU.

Better estimates over midlatitudes during winter are given by the use of Tb23 in the GSMaP_AMSU algorithm. As discussed in Section III-A, Tb23 in the LUT for midlatitudes during winter [Fig. 2(a)] increases more rapidly with rainfall (i.e., large diff_TB23$_{\mathrm{LUT}}$) because there is a smaller amount of water vapor at midlatitudes during winter. Therefore, Tb23 represents rainfall rate more unambiguously over midlatitudes during winter. The path length through which the atmosphere is viewed by cross-track scanners increases with LZA. For LZA $= 60$ (near the limb), Tb23 is still a useful indicator of rain rate over midlatitudes during winter [Fig. 4(c)].

On the other hand, over the subtropical region (5° S–30° S) for July 2005, GSMaP_AMSU gives higher rainfall than three reference algorithms [Fig. 9(d)–(f)], while NOAA_AMSU has good agreement with three reference algorithms. GSMaP_AMSU is developed based on the AMSU/TRMM matched-up cases, most of which are organized rain systems, possibly leading to overestimation of GSMaP_AMSU for scattering rain cases over subtropical regions.

B. Case Studies

In this section, GSMaP_AMSU estimates are compared with NOAA_AMSU estimates, using 75 AMSU/TRMM matched-up cases (44 cases for January 2005 and 31 cases for July 2005). In addition to the rmse and bias, the equitable threat score (ETS) [55], [66] is used for the evaluation of the performance of the RNC of the AMSU algorithms. The ETS ranges from $-1/3$ to 1, and the best possible ETS is 1

$$\mathrm{ETS} = \frac{N_1 - N_{\mathrm{ref}}}{N_1 - N_{\mathrm{ref}} + N_2 + N_3}$$
$$N_{\mathrm{ref}} = \frac{(N_1 + N_2)(N_1 + N_3)}{N_1 + N_2 + N_3 + N_4} \tag{10}$$

where N_1 is the number of pixels where rain is observed by the reference algorithm and the RNC method of the AMSU algorithm (GSMaP_AMSU or NOAA_AMSU) classifies rain, N_2 is the number of pixels where rain is observed by the reference algorithm and the RNC method classifies no rain, N_3 is the number of pixels where rain is not observed by the reference algorithm and the RNC method of the AMSU algorithm classifies rain, and N_4 is the number of pixels where rain is not observed by the reference algorithm and the RNC method classifies no rain. For the ETS, PR2A25, GSMaP_TMI, and TMI2A12 are used for the reference algorithm, but for the rmse and bias, PR2A25 is not used as the reference algorithm. This is because the rain retrieval process of GSMaP_AMSU, except for its RNC, is developed based on comparison with PR2A25 (Fig. 8), and the PR2A25 data are not independent.

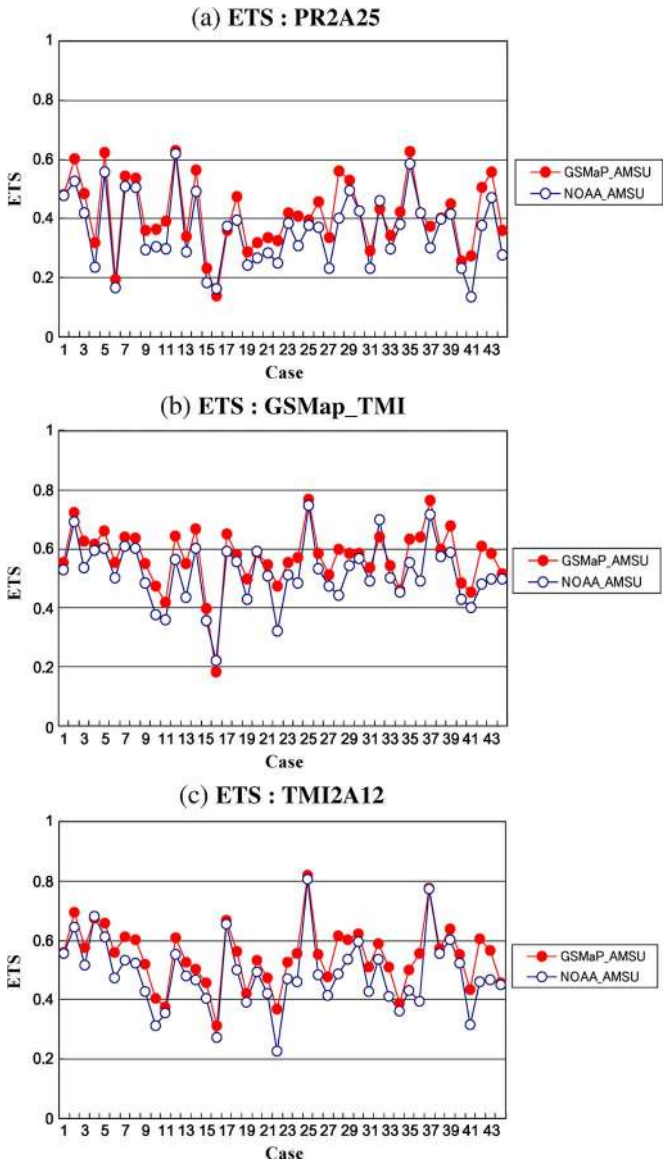

Fig. 10. ETSs of GSMaP_AMSU and NOAA_AMSU for the 44 AMSU/TRMM matched-up cases for January 2005 using (a) PR2A25, (b) GSMaP_TMI, and (c) TMI2A12 as references.

It is seen from Figs. 10 and 11 that the ETSs of GSMaP_AMSU are higher than those of NOAA_AMSU for all three references for most of the cases. Both RNC methods in GSMaP_AMSU and NOAA_AMSU use the AMSU-A data. However, the regionally varying threshold value of Tb31$_{\mathrm{LUT0}}$ is computed in the GSMaP_AMSU algorithm using atmospheric variables given by GANAL, while the AMSU-A cloud liquid water content estimated from Tb23 and Tb31 by assuming an isothermal atmosphere [14], [46], [67] is used by NOAA_AMSU. Assuming an isothermal atmosphere for nonisothermal atmospheres in the AMSU-A cloud liquid water content retrieval

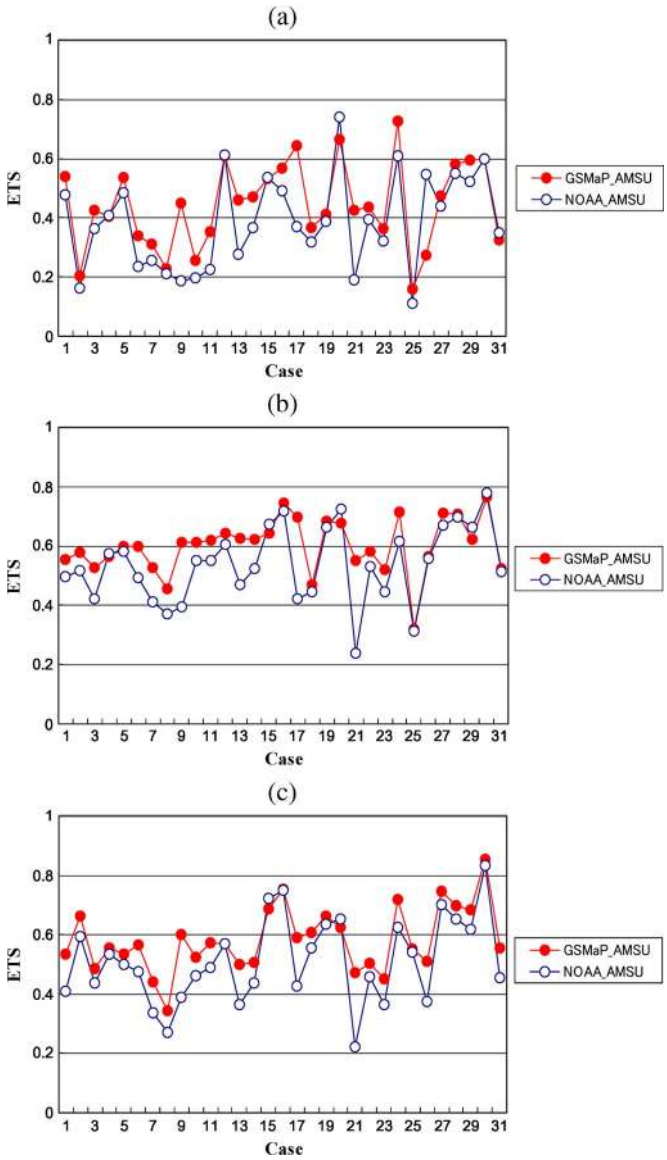

Fig. 11. Same as Fig. 10 except for the 31 AMSU/TRMM matched-up cases for July 2005. (a) ETS: PR2A25. (b) ETS: GSMaP_TMI. (c) ETS: TMI2A12.

might be responsible for larger errors for NOAA_AMSU than for GSMaP_AMSU. The differences are also caused by using SI in GSMaP_AMSU for its RNC.

A recent study [26] showed that the IR interpolation of GSMaP (GSMaP_MVK) is more efficient using rain estimations derived from microwave sounder data based on the NOAA_AMSU algorithm in addition to those derived from microwave imager data. This is caused by the more accurate rain detection by the sounders than the IR sensors that observe cloud-top temperature. Therefore, using the estimates retrieved by GSMaP_AMSU, which has higher rain detection than NOAA_AMSU, may lead to better GSMaP_MVK estimates.

It is seen from Figs. 12(a), 13(a), 14(a), and 15(a) that the rmse and bias of GSMaP_AMSU are lower than those of NOAA_AMSU when GSMaP_TMI is used as a reference. On the other hand, the rmse and, especially, bias of NOAA_AMSU are lower than that for GSMaP_AMSU when TMI2A12 is used as a reference [Figs. 12(b), 13(b), 14(b), and 15(b)]. In

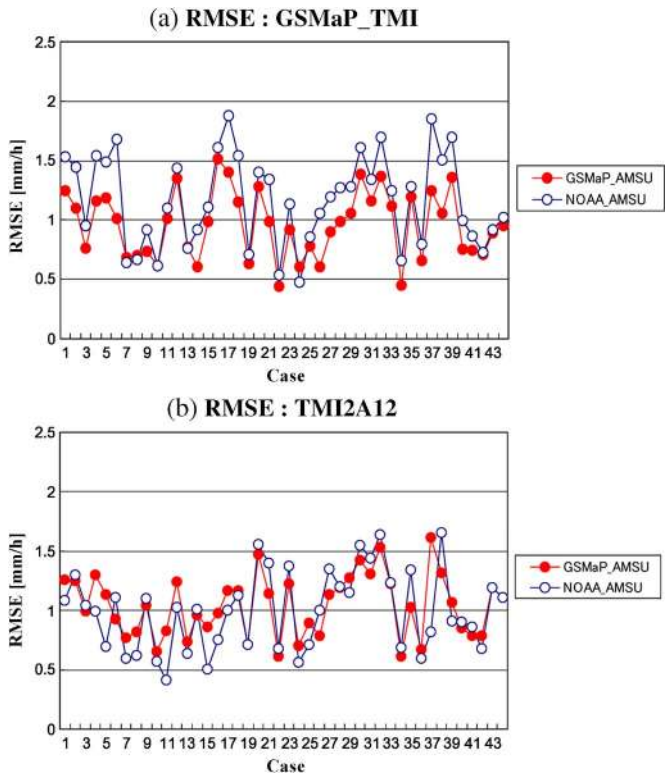

Fig. 12. RMSEs of GSMaP_AMSU and NOAA_AMSU for the 44 AMSU/TRMM matched-up cases for January 2005 using (a) GSMaP_TMI and (b) TMI2A12 as references.

the NOAA_AMSU algorithm, the relationship between surface rain rate and IWP is derived using the TMI2A12 (GPROF) algorithm database. These results suggest that physically consistent algorithms, which share a database or an LUT, should be applied to passive microwave imagers and sounders because consistency in the rain products from passive microwave imagers and sounders is very important in combining them. Development of a rain retrieval algorithm for microwave sounders sharing at a maximum a common algorithm framework with the algorithm for other microwave imagers is also a key issue for the upcoming Global Precipitation Mission [68] where microwave sounders are now considered as important sensors for achieving three-hourly rainfall sampling.

V. Summary and Future Work

Global precipitation maps have been retrieved from passive MWRs currently in orbit such as the TMI, AMSR-E, and SSM/I using the GSMaP_MWR algorithm. Despite the improved rainfall estimates from passive MWRs, the challenge remains to further fill in information gaps through more frequent satellite observations. In this paper, we developed an over-ocean rainfall retrieval algorithm for the AMSU based on the GSMaP MWR algorithm. This algorithm combined an emission-based estimate from Tb at 23 GHz and a scattering-based estimate from Tb at 89 GHz, depending on an SI computed from Tb at both 89 and 150 GHz. Precipitation inhomogeneity was also taken into account.

The GSMaP-retrieved rainfall from the AMSU was compared with the NOAA-standard-algorithm-retrieved data using

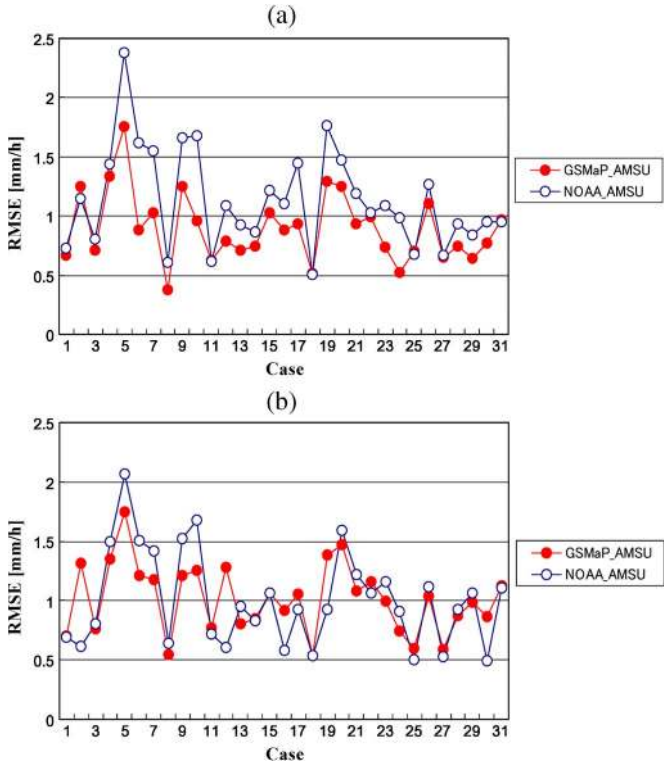

Fig. 13. Same as Fig. 12 except for the 31 AMSU/TRMM matched-up cases for July 2005. (a) RMSE: GSMaP_TMI. (b) RMSE: TMI2A12.

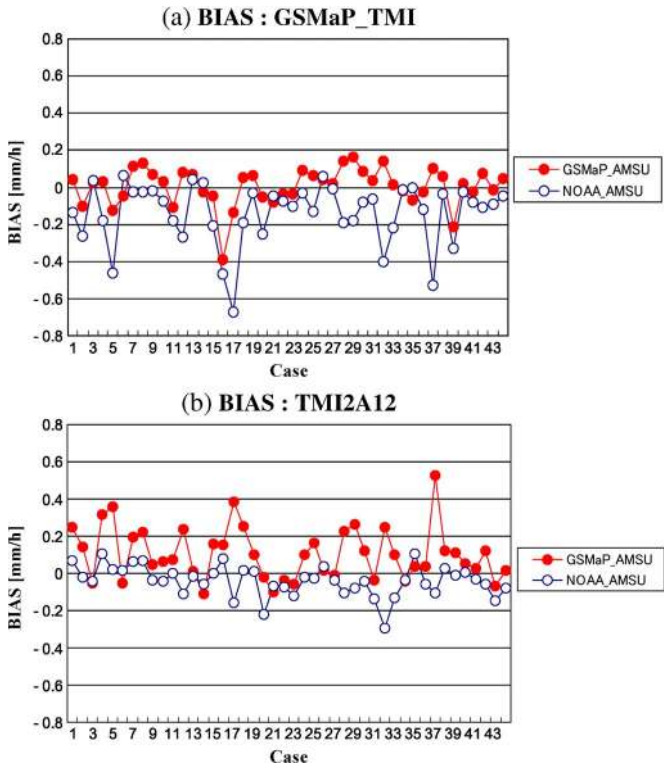

Fig. 14. Bias of GSMaP_AMSU and NOAA_AMSU for the 44 AMSU/TRMM matched-up cases for January 2005 using (a) GSMaP_TMI and (b) TMI2A12 as references.

the TRMM data as a reference. Rain rates retrieved from GSMaP_AMSU have better agreement with TRMM estimates over midlatitudes during winter. Better estimates over midlatitudes during winter were given by the use of Tb at 23 GHz in the GSMaP_AMSU algorithm. On the other hand, GSMaP_AMSU overestimated rain rates over subtropical regions. This is probably because GSMaP_AMSU was developed based on the AMSU/TRMM matched-up cases, most of which are organized rain systems.

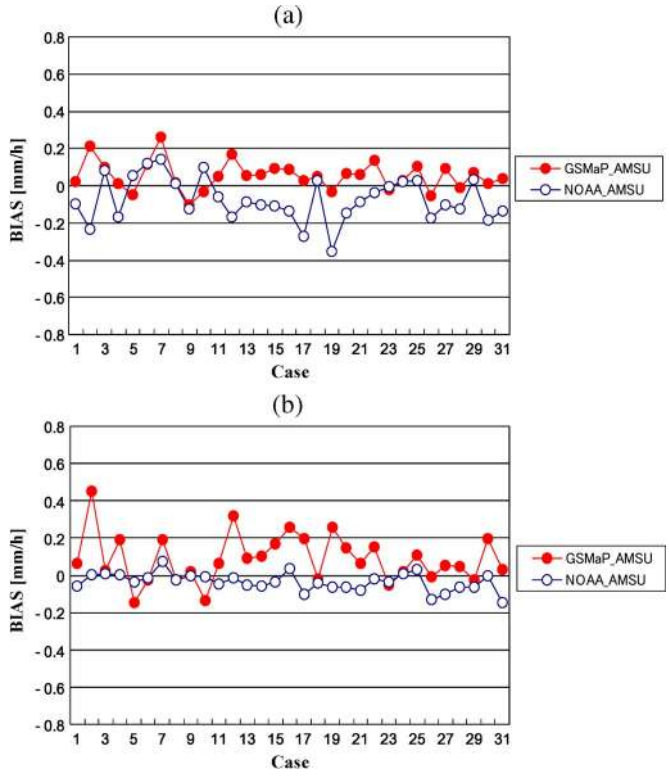

Fig. 15. Same as Fig. 14 except for the 31 AMSU/TRMM matched-up cases for July 2005. (a) Bias: GSMaP_TMI. (b) Bias: TMI2A12.

Comparisons using 75 AMSU/TRMM matched-up cases showed that GSMaP_AMSU had higher rain detection than NOAA_AMSU. Therefore, using the estimates retrieved by GSMaP_AMSU may lead to better GSMaP_MVK estimates. It was also shown that physically consistent algorithms, which share a database or an LUT, should be applied to passive microwave imagers and sounders because consistency in the rain products from passive microwave imagers and sounders is very important in combining them.

Implementing GSMaP_AMSU rain retrieval will bring more accuracy to a GSMaP global rainfall map where AMSU estimates are not used now.

ACKNOWLEDGMENT

The authors would like to thank R. Ferraro from NOAA/NESDIS for providing rain estimates derived from the MSPPS Day-2 algorithm, G. Liu from Florida State University, Tallahassee, for providing his RTM, H. Murata from the JMA for his kind guidance on using the AAPP, T. Manabe from Osaka Prefecture University, Sakai, Japan, for his comments on this paper, and T. Mega from Osaka Prefecture University for the helpful computing assistance. The authors would also like to thank the two anonymous reviewers for their constructive comments.

REFERENCES

[1] C. Kummerow, W. Barnes, T. Kozu, J. Shiue, and J. Simpson, "The Tropical Rainfall Measuring Mission (TRMM) sensor package," *J. Atmos. Ocean. Technol.*, vol. 15, no. 3, pp. 809–817, Jun. 1998.

[2] T. Kawanishi, T. Sezai, Y. Ito, K. Imaoka, T. Takeshima, Y. Ishido, A. Shibata, M. Miura, H. Inahata, and R. W. Spencer, "The Advanced Microwave Scanning Radiometer for the Earth Observing System (AMSR-E), NASDA's contribution to the EOS for global energy and water cycle studies," *IEEE Trans. Geosci. Remote Sens.*, vol. 41, no. 2, pp. 184–194, Feb. 2003.

[3] J. P. Hollinger, J. L. Peirce, and G. A. Poe, "SSM/I instrument evaluation," *IEEE Trans. Geosci. Remote Sens.*, vol. 28, no. 5, pp. 781–790, Sep. 1990.

[4] M. C. Colton and G. A. Poe, "Intersensor calibration of DMSP SSM/I's: F-8 to F-14, 1987–1997," *IEEE Trans. Geosci. Remote Sens.*, vol. 37, no. 1, pp. 418–439, Jan. 1999.

[5] T. Kozu, T. Kawanishi, H. Kuroiwa, M. Kojima, K. Oikawa, H. Kumagai, K. Okamoto, M. Okumura, H. Nakatsuka, and K. Nishikawa, "Development of precipitation radar onboard the Tropical Rainfall Measuring Mission satellite," *IEEE Trans. Geosci. Remote Sens.*, vol. 39, no. 1, pp. 102–116, Jan. 2001.

[6] K. Okamoto, "A short history of the TRMM precipitation radar," *Meteorol. Monogr.*, vol. 29, no. 51, pp. 187–195, Jan. 2003.

[7] K. Okamoto and S. Shige, "TRMM precipitation radar and its observation results," *IEICE Trans. Commun.*, vol. J91-B, no. 7, pp. 723–733, Jul. 2008, (in Japanese).

[8] K. Aonashi, J. Awaka, M. Hirose, T. Kozu, T. Kubota, G. Liu, S. Shige, S. Kida, S. Seto, N. Takahashi, and Y. Takayabu, "GSMaP passive microwave precipitation retrieval algorithm: Algorithm description and validation," *J. Meteorol. Soc. Jpn.*, vol. 87A, pp. 119–136, 2009.

[9] T. Kubota, S. Shige, H. Hashizume, K. Aonashi, N. Takahashi, S. Seto, M. Hirose, Y. N. Takayabu, K. Nakagawa, K. Iwanami, T. Ushio, M. Kachi, and K. Okamoto, "Global precipitation map using satelliteborne microwave radiometers by the GSMaP project: Production and validation," *IEEE Trans. Geosci. Remote Sens.*, vol. 45, no. 7, pp. 2259–2275, Jul. 2007.

[10] T. Ushio, K. Sasashige, T. Kubota, S. Shige, K. Okamoto, K. Aonashi, T. Inoue, N. Takahashi, T. Iguchi, M. Kachi, R. Oki, T. Morimoto, and Z. Kawasaki, "A Kalman filter approach to the Global Satellite Mapping of Precipitation (GSMaP) from combined passive microwave and infrared radiometric data," *J. Meteorol. Soc. Jpn.*, vol. 87A, pp. 137–151, 2009.

[11] T. M. Rickenbach, "Cloud-top evolution of tropical oceanic squall lines from radar reflectivity and infrared satellite data," *Mon. Weather Rev.*, vol. 127, no. 12, pp. 2951–2976, Dec. 1999.

[12] T. Mo, "Prelaunch calibration of the Advanced Microwave Sounding Unit-A for NOAA-K," *IEEE Trans. Microw. Theory Tech.*, vol. 44, no. 8, pp. 1460–1469, Aug. 1996.

[13] R. W. Saunders, T. J. Hewison, S. J. Stringer, and N. C. Atkinson, "The radiometric characterization of AMSU-B," *IEEE Trans. Microw. Theory Tech.*, vol. 43, no. 4, pp. 760–771, Apr. 1995.

[14] R. F. Ferraro, F. Weng, N. Grody, L. Zhao, H. Meng, C. Kongoli, P. Pellegrino, S. Qiu, and C. Dean, "NOAA operational hydrological products derived from the Advanced Microwave Sounding Unit (AMSU)," *IEEE Trans. Geosci. Remote Sens.*, vol. 43, no. 5, pp. 1036–1049, May 2005.

[15] C. Surussavadee and D. H. Staelin, "Global millimeter-wave precipitation retrievals trained with a cloud-resolving numerical weather-prediction model. Part I: Retrieval design," *IEEE Trans. Geosci. Remote Sens.*, vol. 46, no. 1, pp. 99–108, Jan. 2008.

[16] C. Surussavadee and D. H. Staelin, "Global millimeter-wave precipitation retrievals trained with a cloud-resolving numerical weather-prediction model. Part II: Performance evaluation," *IEEE Trans. Geosci. Remote Sens.*, vol. 46, no. 1, pp. 109–118, Jan. 2008.

[17] G. Huffman, R. Adler, D. Bolvin, G. Gu, E. Nelkin, K. Bowman, Y. Hong, E. Stocker, and D. Wolff, "The TRMM Multisatellite Precipitation Analysis (TMPA): Quasi-global, multiyear, combined-sensor precipitation estimates at fine scales," *J. Hydrometeorol.*, vol. 8, no. 1, pp. 38–55, Feb. 2007.

[18] R. J. Joyce, J. E. Janowiak, P. A. Arkin, and P. Xie, "CMORPH: A method that produces global precipitation estimates from passive microwave and infrared data at high spatial and temporal resolution," *J. Hydrometeorol.*, vol. 5, no. 3, pp. 487–503, Jun. 2004.

[19] F. J. Turk and S. Miller, "Toward improving estimates of remotely sensed precipitation with MODIS/AMSR-E blended data techniques," *IEEE Trans. Geosci. Remote Sens.*, vol. 43, no. 5, pp. 1059–1069, May 2005.

[20] F. J. Turk and A. V. Mehta, "Toward improvements in short-time scale satellite-derived precipitation estimates using blended satellite technique," in *Measuring Precipitation From Space—EURAINSAT and the Future*. Berlin, Germany: Springer-Verlag, 2007, pp. 281–290.

[21] C. Kummerow, W. S. Olson, and L. Giglio, "A simplified scheme for obtaining precipitation and vertical hydrometeor profiles from passive microwave sensors," *IEEE Trans. Geosci. Remote Sens.*, vol. 34, no. 5, pp. 1213–1232, Sep. 1996.

[22] C. Kummerow, Y. Hong, W. S. Olson, S. Yang, R. F. Adler, J. McCollum, R. Ferraro, G. Petty, D. B. Shin, and T. T. Wilheit, "The evolution of the Goddard profiling algorithm (GPROF) for rainfall estimation from passive microwave sensors," *J. Appl. Meteorol.*, vol. 40, no. 11, pp. 1801–1820, Nov. 2001.

[23] W. S. Olson, C. D. Kummerow, Y. Song, G. W. Petty, W.-K. Tao, T. L. Bell, S. A. Braun, W. Yansen, S. E. Lang, D. E. Johnson, and C. Chiu, "Precipitation and latent heating distributions from satellite passive microwave radiometry. Part I: Improved method and uncertainty estimates," *J. Appl. Meteorol.*, vol. 45, no. 5, pp. 702–720, May 2006.

[24] T. Wilheit, C. D. Kummerow, and R. Ferraro, "Rainfall algorithms for AMSR-E," *IEEE Trans. Geosci. Remote Sens.*, vol. 41, no. 2, pp. 204–214, Feb. 2003.

[25] *Global Rainfall Map in Near Real Time by JAXA/EORC*. [Online]. Available: http://sharaku.eorc.jaxa.jp/GSMaP/index.htm

[26] T. Kubota, T. Ushio, S. Shige, S. Kida, M. Kachi, and K. Okamoto, "Verification of high resolution satellite-based rainfall estimates around Japan using a gauge-calibrated ground radar dataset," *J. Meteorol. Soc. Jpn.*, vol. 87A, pp. 203–222, 2009.

[27] T. Iguchi, T. Kozu, R. Meneghini, J. Awaka, and K. Okamoto, "Rain profiling algorithm for the TRMM precipitation radar," *J. Appl. Meteorol.*, vol. 39, no. 12, pp. 2038–2052, Dec. 2000.

[28] T. Iguchi, "Spaceborne radar algorithms," in *Measuring Precipitation From Space—EURAINSAT and the Future*, V. Levizzani, P. Bauer, and F. J. Turk, Eds. New York: Springer-Verlag, 2007, pp. 199–212.

[29] T. Iguchi, T. Kozu, J. Kwiatkowski, R. Meneghini, J. Awaka, and K. Okamoto, "Uncertainties in the rain profiling algorithm for the TRMM precipitation radar," *J. Meteorol. Soc. Jpn.*, vol. 87A, pp. 1–30, 2009.

[30] W. Hitschfeld and J. Bordan, "Errors inherent in the radar measurement of rainfall at attenuating wavelengths," *J. Atmos. Sci.*, vol. 11, no. 1, pp. 58–67, Feb. 1954.

[31] R. Meneghini, T. Iguchi, T. Kozu, L. Liao, K. Okamoto, J. A. Jones, and J. Kwiatkowski, "Use of the surface reference technique for path attenuation estimates from the TRMM precipitation radar," *J. Appl. Meteorol.*, vol. 39, no. 12, pp. 2053–2070, Dec. 2000.

[32] T. Iguchi and R. Meneghini, "Intercomparison of single-frequency methods for retrieving a vertical rain profile from airborne or spaceborne radar data," *J. Atmos. Ocean. Technol.*, vol. 11, no. 6, pp. 1507–1516, Dec. 1994.

[33] F. Weng and N. C. Grody, "Retrieval of ice cloud parameters using a microwave imaging radiometer," *J. Atmos. Sci.*, vol. 57, no. 8, pp. 1069–1081, Apr. 2000.

[34] L. Zhao and F. Weng, "Retrieval of ice cloud parameters using the Advanced Microwave Sounding Unit," *J. Appl. Meteorol.*, vol. 41, no. 4, pp. 384–395, Apr. 2002.

[35] D. Vila, R. Ferraro, and R. Joyce, "Evaluation and improvement of AMSU precipitation retrievals," *J. Geophys. Res.*, vol. 112, no. D20, p. D20 119, Oct. 2007. DOI: 10.1029/2007JD008617.

[36] K. Aonashi, A. Shibata, and G. Liu, "An over-ocean precipitation retrieval using SSM/I multichannel brightness temperatures," *J. Meteorol. Soc. Jpn.*, vol. 74, no. 5, pp. 617–637, Oct. 1996.

[37] K. Aonashi and G. Liu, "Passive microwave precipitation retrievals using TMI during the Baiu period of 1999. Part I: Algorithm description and validation," *J. Appl. Meteorol.*, vol. 39, no. 12, pp. 2024–2037, Dec. 2000.

[38] Y. N. Takayabu and M. Katayama, "Low-latitudes rainfall characteristics and its meteorological factors analyzed with mesoscale statistics of TRMM PR data," presented at the 1st Asia Oceania Geosciences Society, Singapore, 2004, Paper 57-OOA-A1683.

[39] Y. N. Takayabu, "Rain-yield per flash calculated from TRMM PR and LIS data and its relationship to the contribution of tall convective rain," *Geophys. Res. Lett.*, vol. 33, no. 18, p. L18 705, Sep. 2006. DOI: 10.1029/2006GL027531.

[40] Y. N. Takayabu, "Observing rainfall regimes using TRMM PR and LIS data," *GEWEX News*, vol. 18, no. 2, pp. 9–10, 2008.

[41] T. Kozu, T. Iguchi, T. Kubota, N. Yoshida, S. Seto, J. Kwiatkowski, and Y. N. Takayabu, "Feasibility of raindrop size distribution parameter estimation with TRMM precipitation radar," *J. Meteorol. Soc. Jpn.*, vol. 87A, pp. 53–66, 2009.

[42] A. Nishitsuji, M. Hoshiyama, J. Awaka, and Y. Furuhama, "An analysis of propagative character at 34.5 GHz and 11.5 GHz between ETS-II satellite and Kasima station—On the precipitation model from stratus," *IEICE Trans. Commun.*, vol. J66-B, no. 9, pp. 1163–1170, Sep. 1983, (in Japanese).
[43] N. Takahashi and J. Awaka, "Introduction of a melting layer model to a rain retrieval algorithm for microwave radiometers," in *Proc. 25th IGARSS*, 2005, pp. 3404–3409.
[44] G. Liu, "A fast and accurate model for microwave radiance calculation," *J. Meteorol. Soc. Jpn.*, vol. 76, no. 2, pp. 335–343, Apr. 1998.
[45] *GSMaP: Global Satellite Mapping of Precipitation*. [Online]. Available: http://www.radar.aero.osakafu-u.ac.jp/~gsmap/
[46] N. Grody, J. Zhao, R. Ferraro, F. Weng, and R. Boers, "Determination of precipitable water and cloud liquid water over oceans from the NOAA 15 Advanced Microwave Sounding Unit," *J. Geophys. Res.*, vol. 106, no. D3, pp. 2943–2954, Feb. 2001. 10.1029/2000JD900616.
[47] C. Guillou, W. Ellison, L. Eymard, K. Lamkaouchi, C. Prigent, G. Delbos, G. Balana, and S. A. Boukabara, "Impact of new permittivity measurements on sea surface emissivity modeling in microwaves," *Radio Sci.*, vol. 33, no. 3, pp. 649–667, May/Jun. 1998.
[48] P. Schluessel and H. Luthardt, "Surface wind speeds over the North Sea from special sensor microwave/imager observations," *J. Geophys. Res.*, vol. 96, no. C3, pp. 4845–4853, Mar. 1991.
[49] R. A. Houze, Jr. and C.-P. Cheng, "Radar characteristics of tropical convection observed during GATE: Mean properties and trends over the summer season," *Mon. Weather Rev.*, vol. 105, no. 8, pp. 964–980, Aug. 1977.
[50] B. Kedem, L. Chiu, and G. North, "Estimation of mean rain rate: Application to satellite observations," *J. Geophys. Res.*, vol. 95, no. D2, pp. 1965–1972, Feb. 1990.
[51] C. Kummerow and L. Giglio, "A passive microwave technique for estimating rainfall and vertical structure information from space. Part I: Algorithm description," *J. Appl. Meteorol.*, vol. 33, no. 1, pp. 3–18, Jan. 1994.
[52] *ATOVS (Advanced TIROS Operational Vertical Sounder) and AVHRR (Advanced High Resolution Radiometer) Pre-processing Package (AAPP)*. [Online]. Available: http://www.metoffice.gov.uk/research/interproj/nwpsaf/aapp/about.html
[53] G. Liu and J. A. Curry, "Retrieval of precipitation from satellite microwave measurements using both emission and scattering," *J. Geophys. Res.*, vol. 97, no. D9, pp. 9959–9974, Jun. 1992.
[54] G. Liu and J. A. Curry, "Large-scale cloud features during January 1993 in the North Atlantic Ocean as determined from SSM/I and SSM/T2 observations," *J. Geophys. Res.*, vol. 101, no. D3, pp. 7019–7032, Mar. 1996.
[55] D. S. Wilks, *Statistical Methods in the Atmospheric Sciences*, 2nd ed. New York: Academic, 2006.
[56] K. M. Lau and H. T. Wu, "Warm rain processes over tropical oceans and climate implications," *Geophys. Res. Lett.*, vol. 30, no. 24, p. 2290, Dec. 2003. DOI:10.1029/2003GL018567.
[57] S. Seto, T. Kubota, N. Takahashi, T. Iguchi, and T. Oki, "Advanced rain/no-rain classification methods for microwave radiometer observations over land," *J. Appl. Meteorol. Climatol.*, vol. 47, no. 11, pp. 3016–3029, 2008.
[58] C. Kongoli, P. Pellegrino, R. Ferraro, H. Meng, and C. Dean, "The utilization of the AMSU high frequency measurements for improved coastal rain retrievals," *Geophys. Res. Lett.*, vol. 34, no. 17, p. L17 809, Sep. 2007. DOI: 10.1029/ 2007GL029940.
[59] W. K. Berg, T. L'Ecuyer, and C. Kummerow, "Rainfall climate regimes: The relationship of regional TRMM rainfall biases to the environment," *J. Appl. Meteorol.*, vol. 45, no. 3, pp. 434–454, Mar. 2006.
[60] G. N. Harris, Jr., K. P. Bowman, and D. Shin, "Comparison of freezing-level altitudes from the NCEP reanalysis with TRMM precipitation radar brightband data," *J. Clim.*, vol. 13, no. 23, pp. 4137–4148, Dec. 2000.
[61] W. K. Berg, C. Kummerow, and C. A. Morales, "Differences between east and west Pacific rainfall systems," *J. Clim.*, vol. 15, no. 24, pp. 3659–3672, Dec. 2002.
[62] J. Ikai and K. Nakamura, "Comparison of rain rates over the ocean derived from TRMM microwave imager and precipitation radar," *J. Atmos. Ocean. Technol.*, vol. 20, no. 12, pp. 1709–1726, Dec. 2003.
[63] T. T. Wilheit, A. T. C. Chang, and L. S. Chiu, "Retrieval of monthly rainfall indices from microwave radiometric measurements using probability distribution functions," *J. Atmos. Ocean. Technol.*, vol. 8, no. 1, pp. 118–136, Feb. 1991.
[64] S. Kida, S. Shige, T. Kubota, K. Aonashi, and K. Okamoto, "Improvement of rain/no-rain classification methods for microwave radiometer observations over ocean using the 37-GHz emission signature," *J. Meteorol. Soc. Jpn.*, vol. 87A, pp. 165–181, 2009.
[65] C. Kummerow, "GPROF_2008 over water and plans for adapting the algorithm for land applications," in *Program Abstr. 4th Int. Workshop Precipitation Retrieval Algorithms Satell. Microw. Radiometer, Radar IR DATA*, 2009, p. 26.
[66] J. T. Schaefer, "The critical success index as an indicator of warning skill," *Weather Forecast.*, vol. 5, no. 4, pp. 570–575, Dec. 1990.
[67] F. Weng, L. Zhao, G. Poe, R. Ferraro, X. Li, and N. Grody, "AMSU cloud and precipitation algorithms," *Radio Sci.*, vol. 38, no. 4, pp. 8068–8079, 2003.
[68] A. Smith, G. Asrar, Y. Furuhama, A. Ginati, C. Kummerow, V. Levizzani, A. Mugnai, K. Nakamura, R. Adler, V. Casse, M. Cleave, M. Debois, J. Durning, J. Entin, P. Houser, T. Iguchi, R. Kakar, J. Kaye, M. Kojima, D. Lettenmaier, M. Luther, A. Mehta, P. Morel, T. Nakazawa, S. Neeck, K. Okamoto, R. Oki, G. Raju, M. Shepherd, E. Stocker, J. Testud, and E. Wood, "International Global Precipitation Measurement (GPM) program and mission: An overview," in *Measuring Precipitation From Space—EURAINSAT and the Future*, V. Levizzani, P. Bauer, and F. J. Turk, Eds. Berlin, Germany: Springer-Verlag, 2007, pp. 611–633.

Shoichi Shige (M'08) received the B.S., M.S., and Ph.D. degrees from Kyoto University, Kyoto, Japan, in 1995, 1997, and 2001, respectively.

From 2001 to 2004, he was with the Earth Observation Research Center, Japan Aerospace Exploration Agency, as an Invited Scientist. Since 2004, he has been with the Department of Aerospace Engineering, Osaka Prefecture University, Sakai, Japan, where he is currently an Assistant Professor. His research interests include mesoscale convective systems and satellite rainfall and heating profile estimation.

Dr. Shige is a member of the Meteorological Society of Japan, American Meteorological Society, American Geophysical Union, and Remote Sensing Society of Japan.

Tomoya Yamamoto received the M.E. degree in aerospace engineering from Osaka Prefecture University, Sakai, Japan, in 2009.

He is currently with the Department of Aerospace Engineering, Osaka Prefecture University. His research interests include algorithm development for spaceborne microwave radiometers and validation of rainfall retrievals.

Takeaki Tsukiyama received the B.E. degree in aerospace engineering from Osaka Prefecture University, Sakai, Japan, in 2008.

He is currently with the Department of Aerospace Engineering, Osaka Prefecture University. His research interests include algorithm development for spaceborne microwave radiometers and validation of rainfall retrievals.

Satoshi Kida received the B.E. and M.E. degrees in aerospace engineering from Osaka Prefecture University, Sakai, Japan, in 2005 and 2007, respectively.

He is currently with the Department of Aerospace Engineering, Osaka Prefecture University. His research interests include algorithm development for spaceborne microwave radiometers and validation of rainfall retrievals.

Hiroki Ashiwake received the B.E. degree in aerospace engineering from Osaka Prefecture University, Sakai, Japan, in 2008.

He is currently with the Department of Aerospace Engineering, Osaka Prefecture University. His research interests include algorithm development for spaceborne microwave radiometers and validation of rainfall retrievals.

Takuji Kubota (M'07) received the B.S., M.S., and Ph.D. degrees from Kyoto University, Kyoto, Japan, in 1999, 2001, and 2004, respectively.

From 2004 to 2005, he was with the Disaster Prevention Research Institute, Kyoto University, as a Postdoctoral Fellow. From 2005 to 2007, he was a Japanese Science Technology Agency Researcher. Since 2007, he has been with the Earth Observation Research Center, Japan Aerospace Exploration Agency, Tsukuba, Japan, as a Researcher. His current research interests include algorithm development for spaceborne microwave radiometers and radars, and validation of rainfall retrievals.

Dr. Kubota is a member of the Remote Sensing Society of Japan, Meteorological Society of Japan, American Meteorological Society, and American Geophysical Union.

Shinta Seto received the B.Sc., M.Sc., and Ph.D. degrees from The University of Tokyo, Tokyo, Japan, in 1998, 2000, and 2003, respectively.

From 2003 to 2006, he was with the National Institute of Information and Communications Technology (formerly the Communications Research Laboratory), Tokyo, as a Postdoctorate Researcher, and he worked on the development of spaceborne dual-frequency precipitation radar. Since 2006, he has been with the Institute of Industrial Science, The University of Tokyo. His current research interests include precipitation retrieval using microwave remote sensing and its application to water cycle studies.

Kazumasa Aonashi received a Bachelor degree from Meteorological College, Kashiwa, Japan, in 1982 and the Ph.D. degree in meteorology from The University of Tokyo, Tokyo, Japan, in 1997.

Since 1988, he has been with the Forecast Research Department, Meteorological Research Institute, Tsukuba, Japan. His areas of expertise include passive microwave precipitation retrieval and assimilation of satellite microwave radiometer data into cloud-resolving numerical weather prediction models.

Ken'ichi Okamoto (M'83) was born in Akashi, Japan, in 1946. He received the Dr. Sci. degree from The University of Tokyo, Tokyo, Japan, in 1973.

He joined the Communications Research Laboratory (CRL, currently the National Institute of Information and Communications Technology), Tokyo, in 1973. He was the Associate Director General of CRL in 1999. He was with Osaka Prefecture University, Sakai, Japan, as a Professor of aerospace engineering from 2000 to 2008. He has been with Tottori University of Environmental Studies, as a Professor of environmental management since 2008 in the Faculty of Environmental and Information Studies. He has been engaged in research on remote sensing of the Earth's environment by various types of radars, including the Tropical Rainfall Measuring Mission precipitation radar.

Dr. Okamoto was the Chair of the domestic International Union of Radio Science-F in Japan in 1997–2000, and he was the Chair of the IEEE Geoscience and Remote Sensing Chapter of the Japan Council in 1998–2000. He was the President of the Remote Sensing Society of Japan in fiscal years 2004 and 2005.